Supporting Information

Fe–single atom catalysts facilitate fast electron transfer with MoS_2/SnS_2 cathode in lithium–sulfur batteries

Kirankumar Venkatesan Savunthari[a,b*], Aswin kumar Anbalagan[c], Kevin Yang[d], Pranathi Garlapati[a], Cherno Jaye[e], Conan Weiland[e], Andrew L. Walter[c*], Sanjeev Mukerjee[a*]

[a]*Department of Chemistry and Chemical Biology, Northeastern University, Boston, Massachusetts 02115, United States*

[b]*Battery Research Institute and Department of Chemistry, Marshall University, Huntington, West Virginia 25755, United States*

[c]*National Synchrotron Light Source II, Brookhaven National Laboratory, Upton, New York 11973, United States*

[d]*Department of Chemical Engineering, Northeastern University, Boston, Massachusetts 02115, United States*

[e]*Material Measurement Laboratory, National Institute of Standards and Technology, Gaithersburg, Maryland 20899, United States*

Corresponding authors: kiran.chemistry1810@gmail.com (K. V. Savunthari); awalter@bnl.gov (A. L. Walter); s.mukerjee@northeastern.edu (S. Mukerjee)

Experimental Part

Preparation of MoS_2/SnS_2 Nanosheets

The MoS_2/SnS_2 nanosheets were fabricated by a one-spot hydrothermal technique. Briefly, it involves the use of 0.5 mmol of ammonium molybdate tetrahydrate and 0.5 mmol of anhydrous tin dichloride as precursors and thiourea as the sulfur source. The precursor solutions and thiourea were dissolved in 35 mL of distilled water (DI), sonicated for 0.5 h, and the resulting solution was then transferred into a Teflon-lined autoclave. After hydrothermal treatment at 220 ^oC for 18 h, the product was allowed to cool to room temperature, then washed with DI water and ethanol, and subsequently dried at 60 ^oC for 12 h under vacuum conditions.

In comparison, MoS_2 nanosheets were synthesized using a similar method, but with only ammonium molybdate tetrahydrate (1 mmol) precursors and thiourea.

Synthesis of Fe-N-C Single-Atom Catalysts (Fe-SACs)

The Fe-SACs were prepared via a facile scalable method. Zinc oxide was heat-treated at 330 ^oC for 1 h in air before use. 0.81 g zinc oxide, 1.64 g 2-methylimidazole, and 0.053 g ammonium sulfate were ball-milled in the presence of 10 µL of methanol for 2 h in a 37.5 mL polypropylene vial with five 3/8-inch methacrylate balls using a SPEX™ SamplePrep 8000M. Zinc Oxide and ammonium sulfate were supplied by Sigma Aldrich and 2-methylimidazole was supplied by Alfa Aesar. 0.0435 g iron (II) acetate and 0.60 g of 1,10-phenanthroline monohydrate were added and ball-milled for 2 h. Iron (II) acetate was supplied from Sigma-Aldrich and 1,10-phenanthroline was supplied from Alfa Aesar. The resulting light pink solid was then subjected to heat treatment in argon at 900 ^oC for 1 h at a ramp rate of 5 $^oC\ min^{-1}$. The resulting Fe-N-C was then ball milled for 5 min with twice its mass of ammonium chloride in a 37.5 mL vial with three methacrylate balls. The mixture was then subjected to a second

heat treatment in argon at 950 °C for 2 h with a ramping rate of 25 °C min^{-1} (0.7 g to 0.8 g) of Fe-N-C was yielded.

Synthesis of S@MoS_2, S@MoS_2/SnS_2, and S@Fe-MoS_2/SnS_2 Materials

The melt-diffusion technique was used to synthesize the S@MoS_2, S@MoS_2/SnS_2, and S@Fe-MoS_2/SnS_2 materials (Fig. 2a).[26] A mixture of S powder and prepared catalysts (MoS_2 or MoS_2/SnS_2 or Fe-SACs + MoS_2/SnS_2 with a mass ratio of 1.5+1.5)) in the ratio of 7:3 was thoroughly ground and then sealed in a glass tube. Subsequently, the mixture was heated under an argon (Ar) atmosphere at 155 °C for 6 h.

Materials Characterization

The pure phases were confirmed by powder X-ray diffraction (XRD, Rigaku Ultima-IV) using Cu-Kα radiation at 44 mA and 40 kV. Raman spectroscopy analysis of the samples was acquired through Horiba Scientific BX43F using an excitation wavelength of 432 to 732 nm. The morphology of the as-prepared materials was determined through transmission electron microscopy and scanning transmission electron microscope (TEM and STEM, Thermofisher Titan Themis 300 S/TEM, 300kV). Thermogravimetric analysis (TGA) was carried out using a TA Instruments SDT Q600 thermal analyzer with a nitrogen (N_2) flow. The variations in the chemical species of the samples under different conditions were studied by Hard X-ray photoelectron microscopy (HAXPES) on the soft and tender X-ray beamline (7-ID-2 (SST-2)) operated by the National Institute of Standards and Technology (NIST) at National Synchrotron Light source II (NSLS II), Brookhaven National Laboratory (BNL). The HAXPS measurements were carried out by utilizing three different incident photon energies, such as 900, 2000, 6000 eV to probe different depths onto the sample surface. To avoid the interaction of the air before loading the samples into the HAXPES chamber, sample bars were transferred into the load lock chamber using an inert transfer system, and the samples were

kept in overnight under ultrahigh environment before starting the measurement. At the HAXPES end station, the incident angle is fixed at 10° and the take-off angle is fixed at 80° for all the samples, irrespective of different incident energies employed. Au foil was used for the calibration purpose and the background of all the spectra were subtracted using a Shirley function. The variations in the electron structure of the samples were examined using Near-edge X-ray absorption fine structure (NEXAFS) measurements of Fe $L_{2,3}$, N -K, C -K and S -K absorption edges, respectively, at the beamlines 7-ID-1 (SST-1) & 7-ID-2 (SST-2) of the NSLS II facility at BNL. The samples were also transferred into the NEXAFS load lock chamber under an inert environment. The samples were measured at an incident angle of 55° to the X-ray polarised beam. All the NEXAFS measurements were collected in total electron yield (TEY) mode, except those for S -K edges measured at SST-2 end station. The S *K*-edge spectra were measured in partial electron yield (PEY) mode. The analysis and quantification of the HAXPES and NEXAFS data were carried out using XPSpeak41 and Athena software, respectively.

Coin-Cell Assembly and Electrochemical Analysis of LSBs

To fabricate cathode electrodes, the as-prepared samples (Pure S, S@MoS_2, S@ MoS_2/SnS_2, and S@Fe-MoS_2/SnS_2), along with Ketjen black as conductive carbon, and polyvinylidene fluoride (PVDF) as a binder, were blended in a weight ratio of 8:1:1 using N-methyl-2-pyrrolidinone (NMP) as a solvent, employing a speed mixture (THINKY AR-250) for 20 min. Then, a 20 μL slurry was drop-casted onto the carbon paper and dried at 60 ^oC for 12 h under vacuum conditions. The weight-loading of S active materials ranged from approximately 2.0 mg/cm^2 to 2.5 mg/cm^2. The LSBs (2032-type) coin cells were constructed by utilizing the as-prepared different cathodes such as Pure S, S@MoS_2, S@MoS_2/SnS_2, and S@Fe-MoS_2/SnS_2, Celgard 2325 membrane and glass fiber as the separator, and Li metal

anode within an Ar-filled glovebox. The electrolyte employed was 1 M lithium bis(trifluoromethanesulfonyl)imide (LiTFSI) in a mixed solvent of 1,3-dioxolane (DOL) and 1,2-dimethoxyethane (DME) (volume ratio 1:1), supplemented with a 2 wt% lithium nitrate ($LiNO_3$) additive. Galvanostatic discharge and charge process were conducted using Arbin Instruments BT-2143 within a voltage range of 1.7 to 2.8 V (vs. Li^+/Li). Current density and specific capacities were determined based on the S weight. Electrochemical impedance spectroscopy (EIS) and cyclic voltammetry (CV) were recorded on AUTOLAB Instruments PGSTAT302N and VoltaLab PGZ 402 electrochemical workstations.

Ex Situ Analysis of LSBs

For *ex situ* analysis, the LSB cells were disassembled after the first cycle (discharge and charge at 0.05 C) and following 1000 cycles at 0.2 C, utilizing S@Fe-MoS_2/SnS_2 cathodes, all within an Ar-filled glovebox. The disassembled electrodes were subsequently dried inside the glovebox. The various electrodes, including pristine, 1st discharge, 1st charge, and after 1000 cycles of S@Fe-MoS_2/SnS_2 cathodes, were analyzed using powder XRD, Raman spectra, HAXPES, and NEXAFS instruments to observe the formation and deformation of Li_2S discharge products during the discharge and charge process of LSBs.

In Situ Operando Raman Spectroscopy Analysis of LSBs

In situ operando Raman analysis was employed to investigate the redox reactions of LSBs and observe the LiPSs using S@Fe-MoS_2/SnS_2 cathode. A 10 μL (S@Fe-MoS_2/SnS_2) slurry was drop-casted onto the Celgard 2325 membrane, and dried at room temperature for 72 h, and the weight-loading S active materials ranged from around 1.0 mg to 1.5 mg. The *in situ* operando Raman measurement cell (ECC-Opto-10 from EL-Cell) was assembled with Li metal anode, glass fiber, 15 μL liquid electrolyte (1M LiTFSI in a solvent of DOL and DME (1:1) with 2 wt% of $LiNO_3$), Celgard 2325 with cathode, aluminum current collector, and 0.2 mm

thick sapphire serving as an optical window (for observing the LiPSs during the discharge and charge processes), all within an Ar-filled glovebox. *In situ* operando Raman spectroscopy experiments were performed by Raman microscope (Horiba Scientific BX43F) equipped with a 50x objective lens (laser wavelength ranging from 473 nm to 732 nm). The system related to galvanostatic discharge/charge tests using AUTOLAB Instruments BOOSTER10A within a voltage range from 1.7 V to 2.8 V (vs. Li^+/Li) at room temperature.

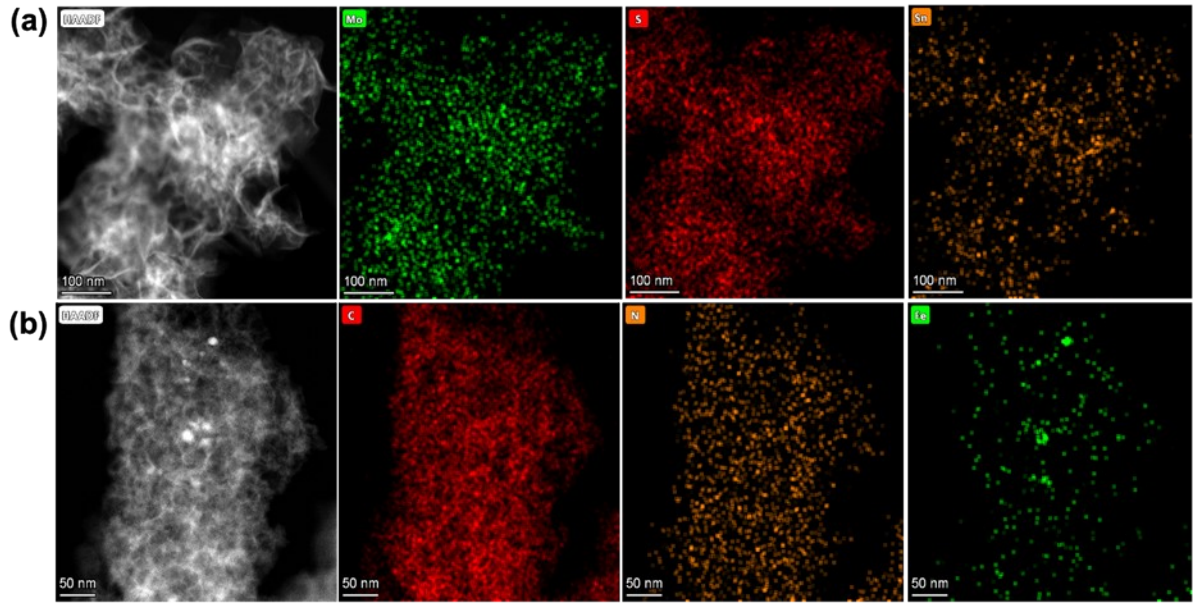

Fig. S1. HAADF-STEM-EDX mapping images of (a) MoS_2/SnS_2 and (b) Fe-N-C SACs.

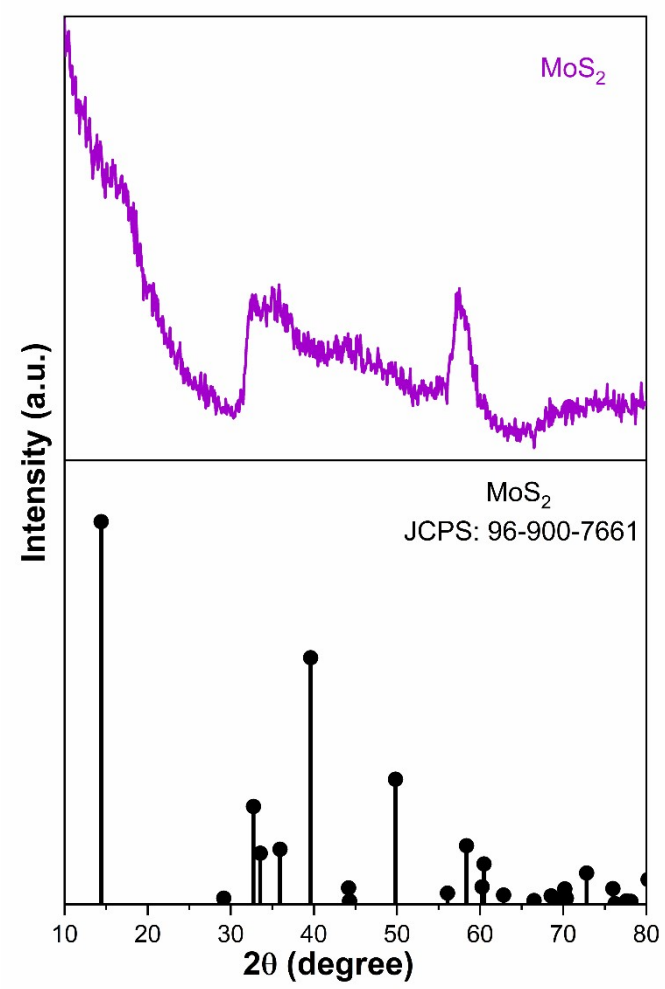

Fig. S2. Powder XRD pattern of MoS_2 nanosheet.

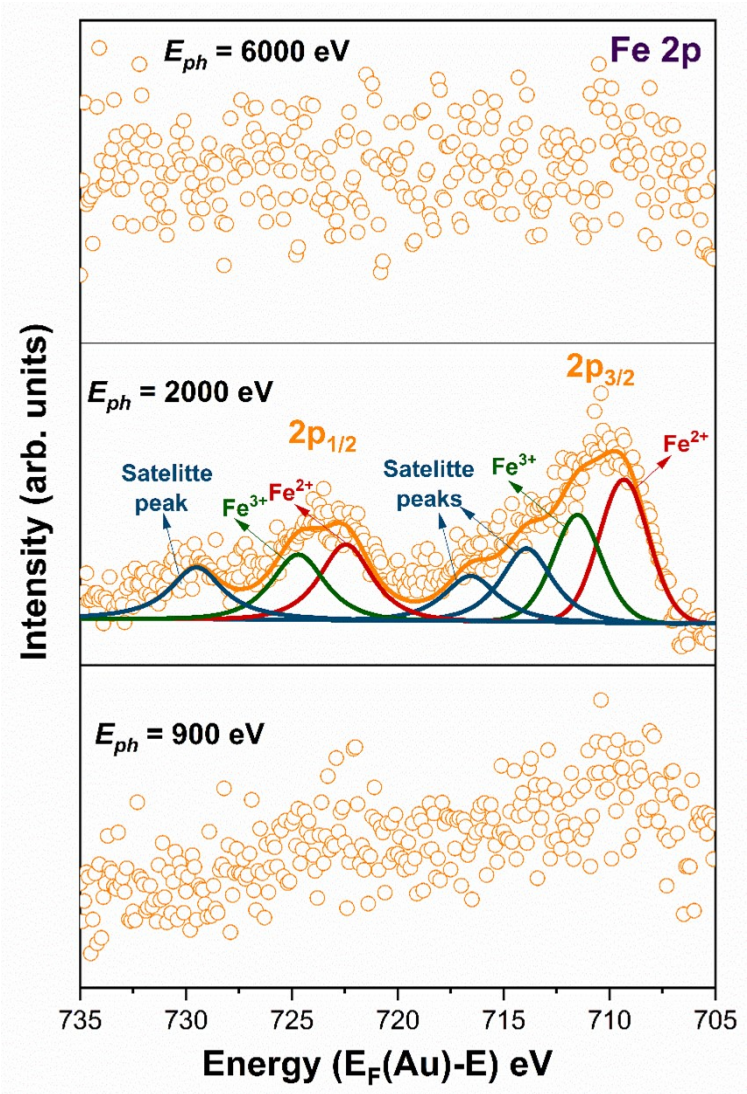
E_{ph} = 6000 eV
Fe 2p
E_{ph} = 2000 eV
$2p_{3/2}$
$2p_{1/2}$
Satelitte peak
Fe^{3+}
Fe^{2+}
Satelitte peaks
Fe^{3+}
Fe^{2+}
E_{ph} = 900 eV
Intensity (arb. units)
735
730
725
720
715
710
705
Energy (E_F(Au)-E) eV

Fig. S3. HAXPES analysis of Fe-N-C SACs presents Fe 2*p* using the 900 eV, 2000 eV, and 6000 eV photon energies (E_{ph}).

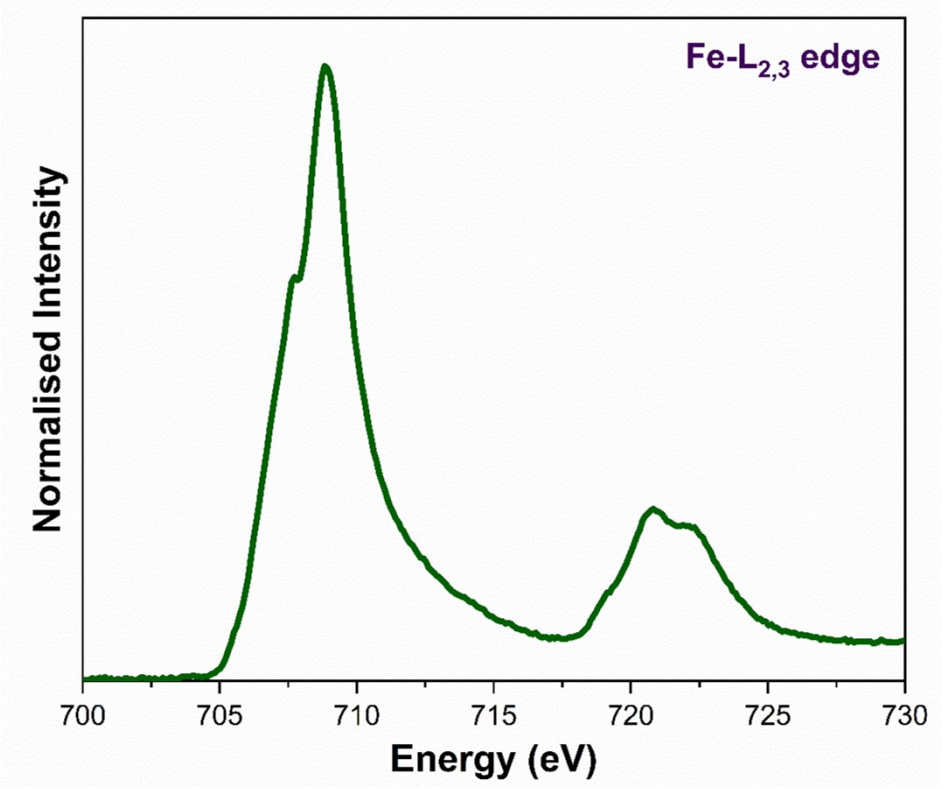

Fig. S4. NEXAFS spectra of Fe $L_{2,3}$ edges of Fe-N-C SACs.

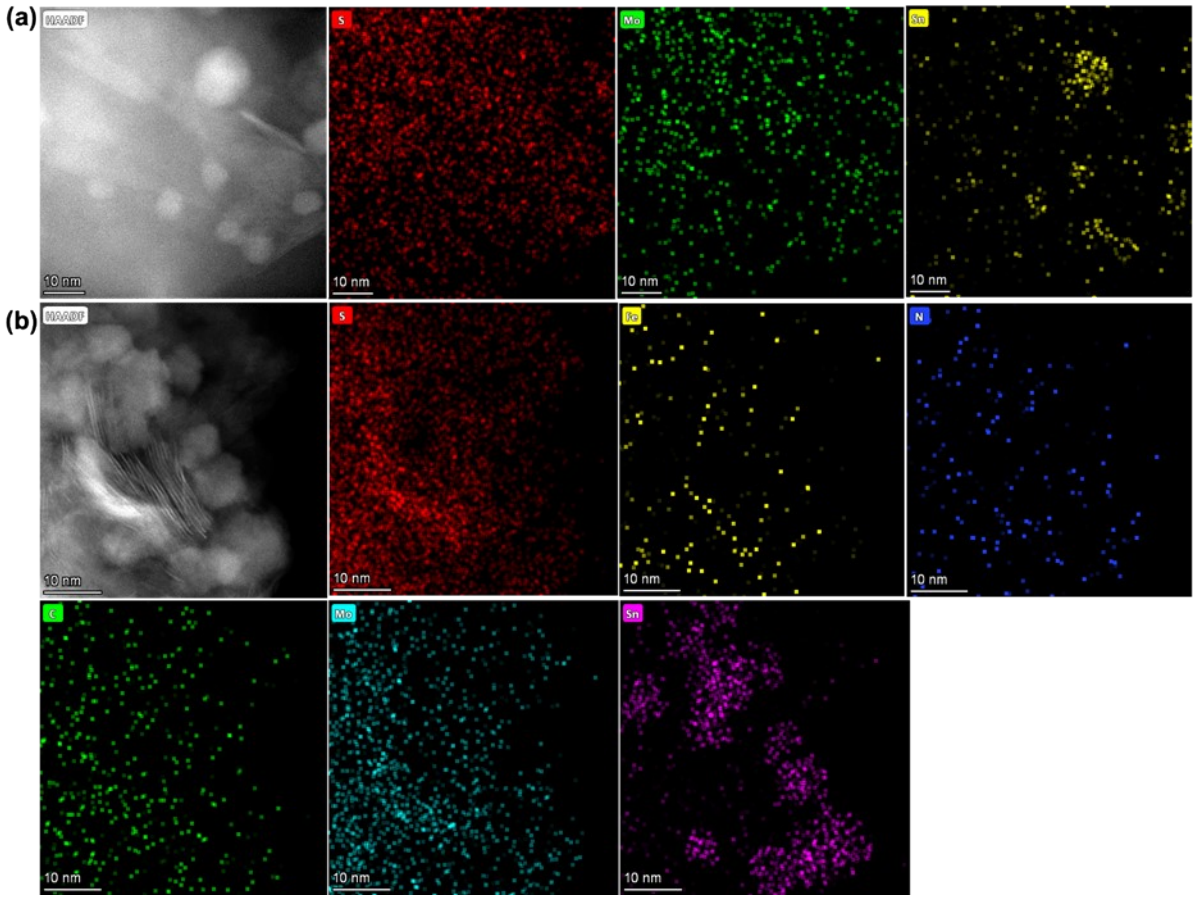
(a)
HAADF
S
Mo
Sn
10 nm
(b)
HAADF
S
Fe
N
C
Mo
Sn
10 nm

Fig. S5. HAADF-STEM-EDX mapping images of (a) S@MoS_2/SnS_2 and (b) S@Fe-MoS_2/SnS_2 samples.

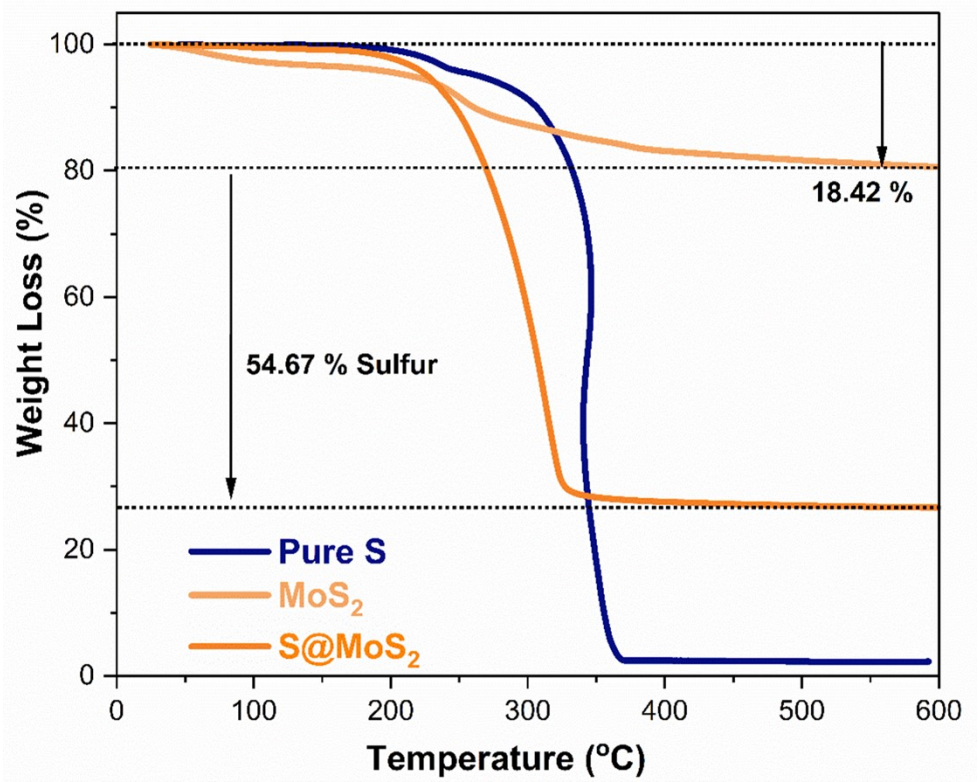

Fig. S6. TGA analysis of S@MoS_2 samples.

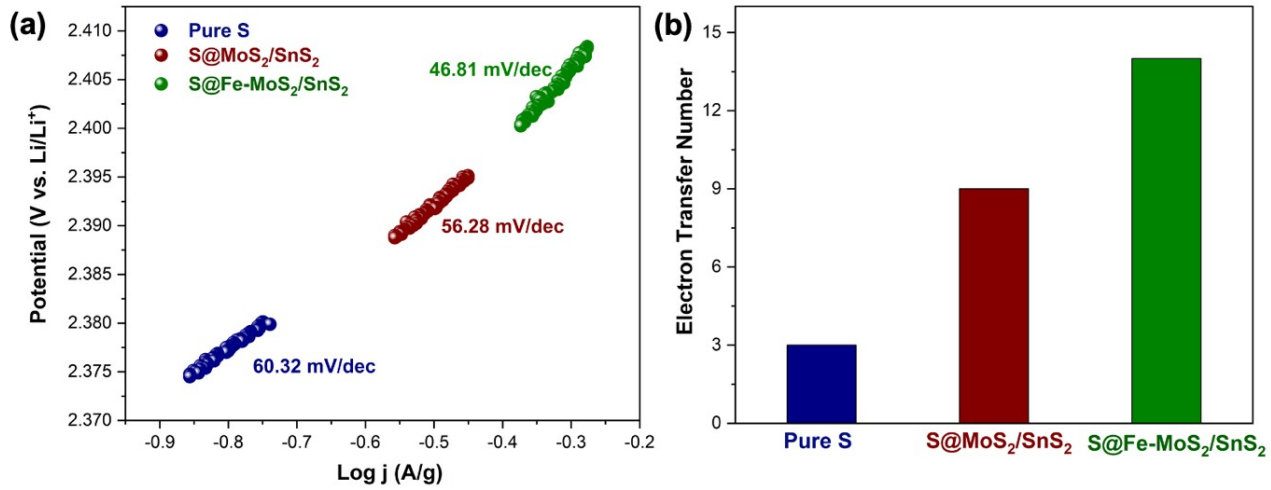

Fig. S7 (a) Tafel slope and (b) An electron transfer number comparison with pure S, S@MoS_2/SnS_2, and S@Fe–MoS_2/SnS_2 cathodes.

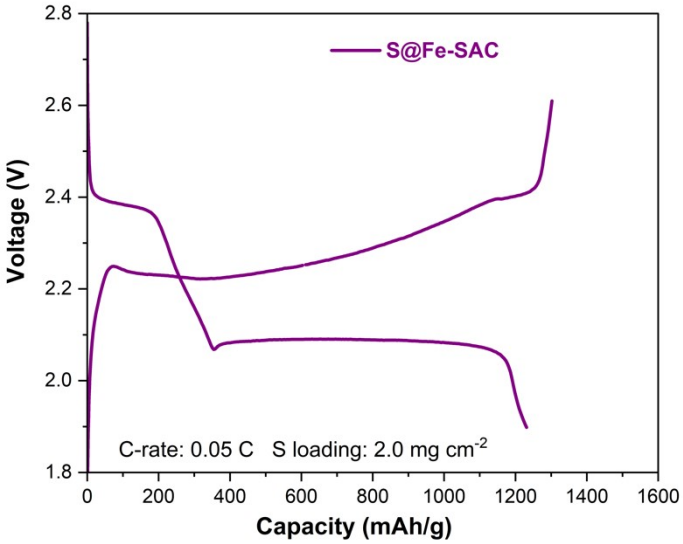

Fig. S8. Galvanostatic initial discharge/charge plots of S@Fe-NC cathode at 0.05 C.

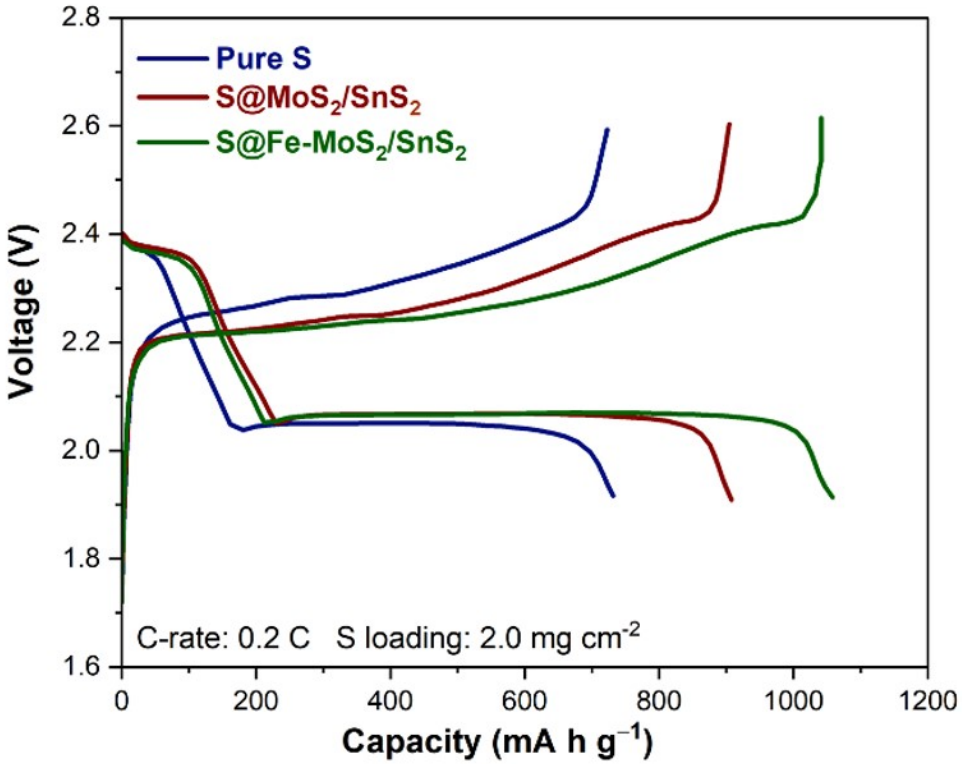

Fig. S9. Galvanostatic initial discharge/charge plots of Pure S, S@MoS_2/SnS_2, and S@MoS_2/SnS_2 cathodes at a current rate of 0.2 C.

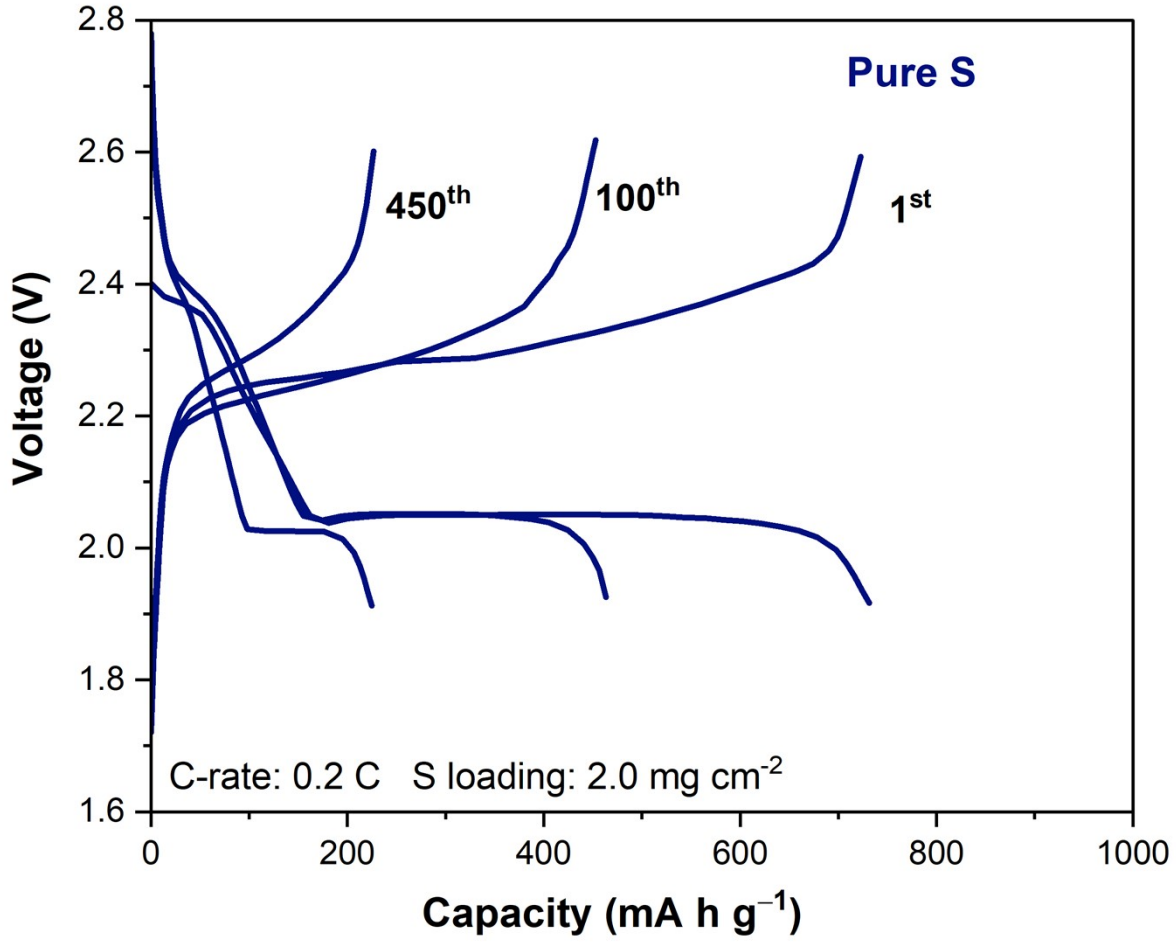

Fig. S10. Different discharge/charge profiles for 1st, 100th, and 450th cycles of Pure S cathode at a current rate of 0.2 C.

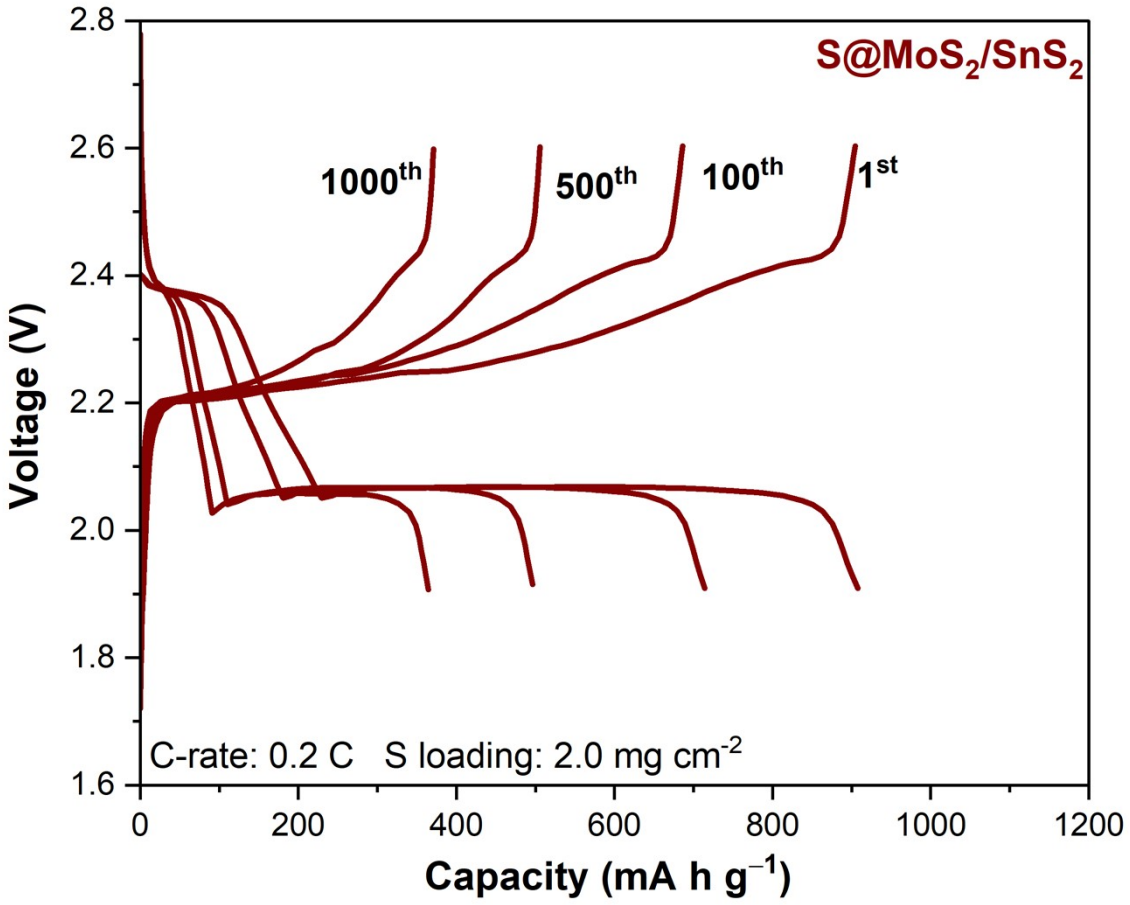

Fig. S11. Different discharge/charge profiles for 1st, 100th, 500th, and 1000th cycles of $S@MoS_2/SnS_2$ cathode at a current rate of 0.2 C.

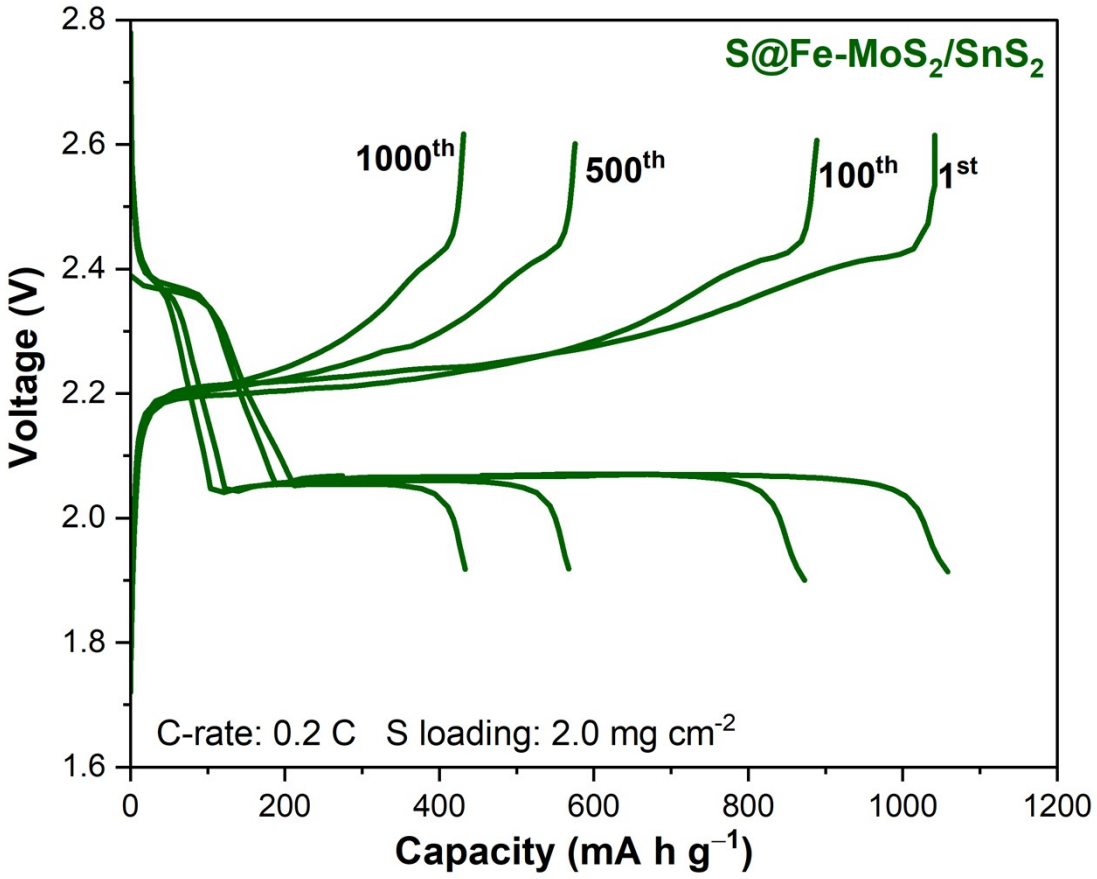

Fig. S12. Different discharge/charge profiles for 1st, 100th, 500th, and 1000th cycles of S@Fe-MoS_2/SnS_2 cathode at a current rate of 0.2 C.

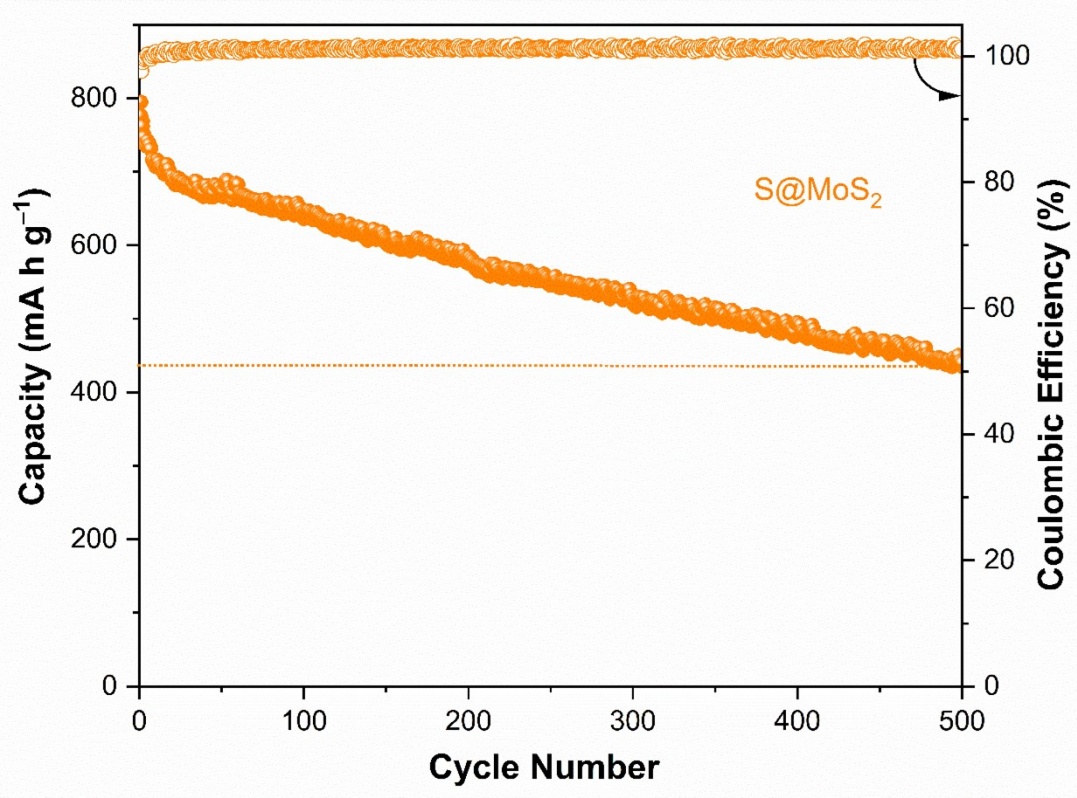

Fig. S13. Long-term cycling stability of the S@MoS_2 cathodes at a current rate of 0. 2 C.

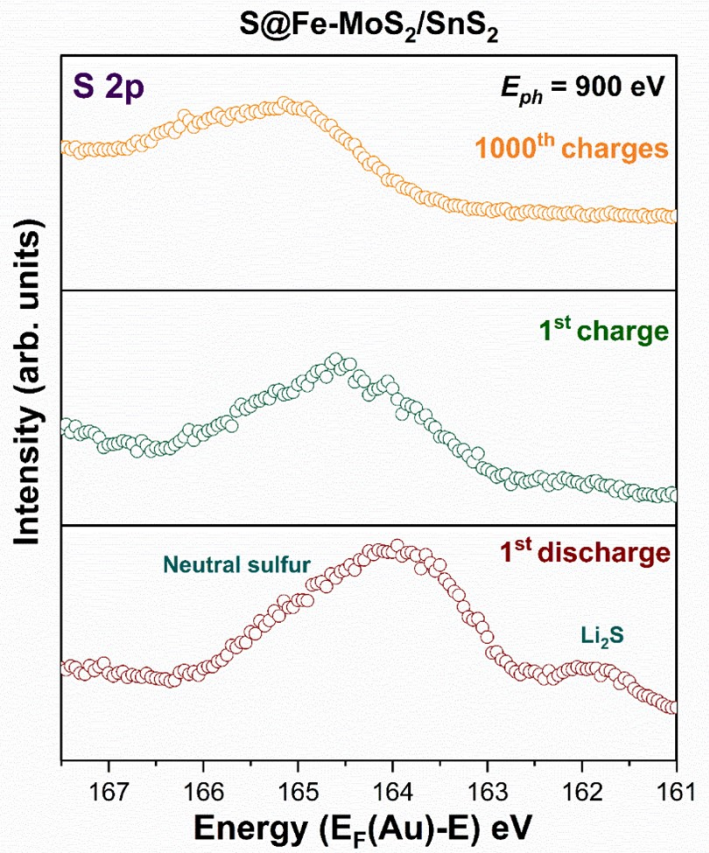

Fig. S14. *Ex Situ* analyses of the S@Fe-MoS_2/SnS_2 cathodes in LSBs, including the 1st discharge, 1st charge, and 1000th charge measurements of HAXPES spectra using S 2*p* element at E_{ph}= 900 eV.

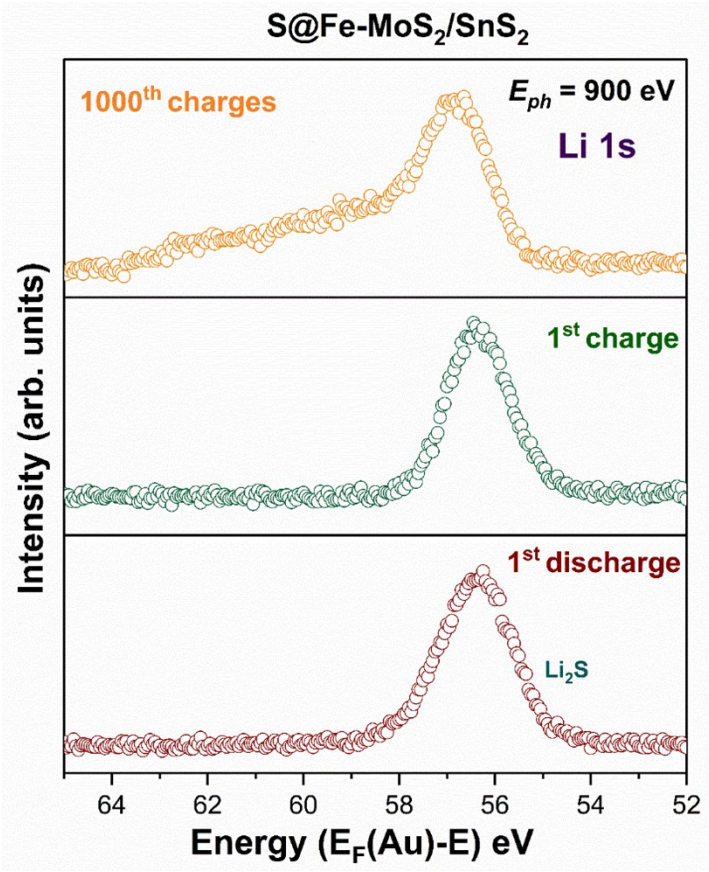

Fig. S15. *Ex Situ* analyses of the S@Fe-MoS_2/SnS_2 cathodes in LSBs, including the 1st discharge, 1st charge, and 1000th charge measurements of HAXPES spectra using Li 1*s* element at E_{ph}= 900 eV.

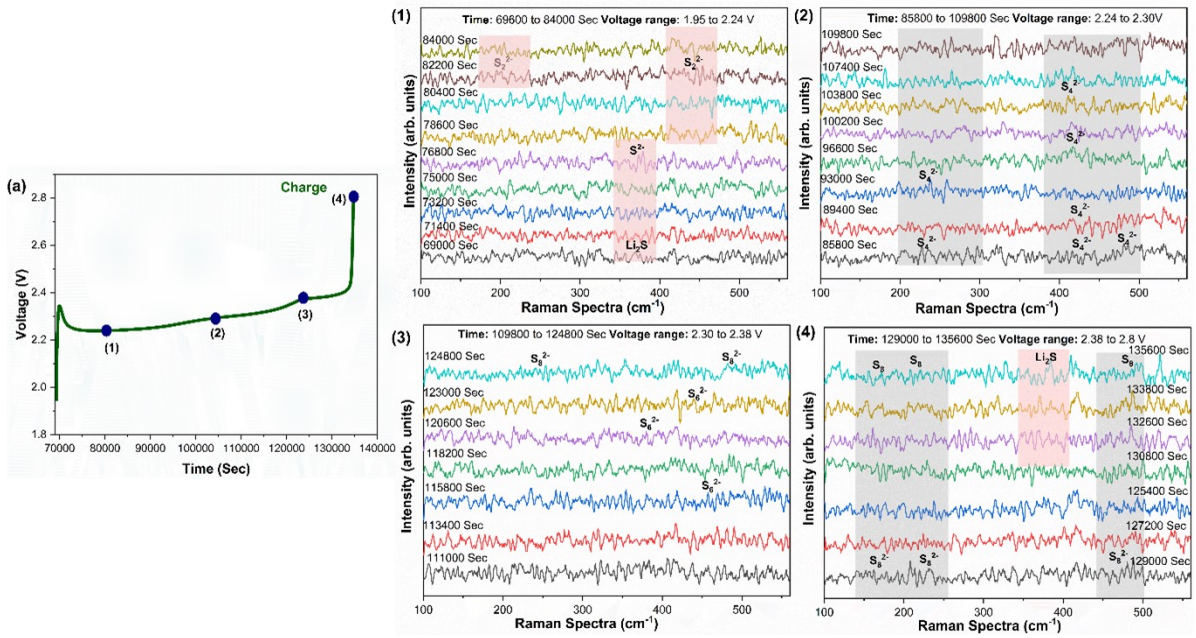

Fig. S16. *In Situ* operando Raman spectra of S@Fe-MoS_2/SnS_2 cathode obtained from LSBs during the first cycle charge (current rate of 0.05 C): a) charge plateaus (voltage range: 1.98 V to 2.8 V and time: 69000 Sec to 135600 Sec) with different spots.

When the LSBs are charged, these reactions are reversible (Li_2S ⇄ long-chain LiPSs ⇄S_8), and the results are given in Figure S14. During the initial cycle of LSBs at a charging rate of 0.05 C, distinct charge plateaus were identified within a voltage range of 1.95 V to 2.24 V over a duration spanning from 69600 Sec to 135600 Sec. Four significant points were delineated from these charge plateaus: At spot (1), the transition involved the insoluble discharge product Li_2S transforming into Li_2S_2 solid, indicating solid formation. This occurred within the voltage range of 1.95 V to 2.24 V and lasted from 69600 Sec to 84000 Sec. Spot (2) marked the conversion of Li_2S_4 to Li_2S_6 in a liquid state, indicating a liquid formation process. This

transformation occurred within the voltage range of 2.24 V to 2.30 V and took place from 85800 Sec to 109800 Sec. At spot (3), the progression involved Li_2S_6 transitioning into Li_2S_8 in a liquid state, again suggesting liquid formation. This transition spanned a voltage range of 2.30 V to 2.38 V and lasted from 109800 Sec to 1248000 Sec. Finally, at spot (4), the transformation from Li_2S_8 to a mixture of S_8 and Li_2S in a liquid-solid state marked another instance of solid formation. This occurred within the voltage range of 2.38 V to 2.80 V over 129000 Sec to 135600 Sec. Furthermore, analysis of the first charged cathode revealed a Li_2S peak, indicating that the Li_2S discharge product may persist partially in initial LSBs cycles. Similar findings from *ex situ* analysis corroborated this observation.

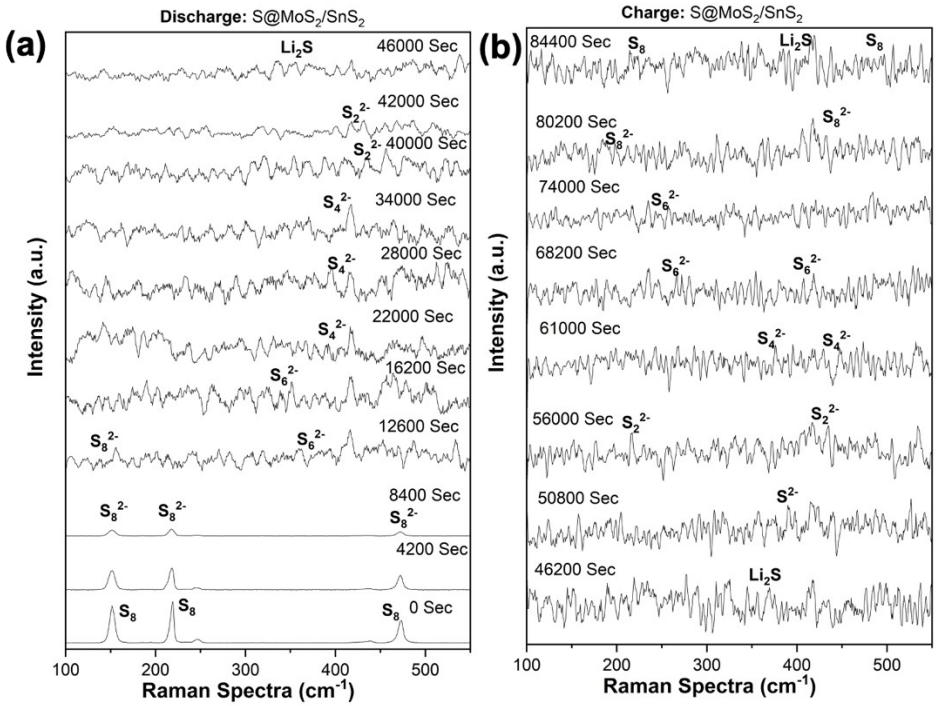

Fig. S17. *In Situ* operando Raman spectra of S@MoS_2/SnS_2 cathode obtained from LSBs during the first cycle discharge (discharge voltage range: 2.38 V to 1.70 V and time: 0 Sec to 46000 Sec) and charge (charge voltage range: 1.98 V to 2.8 V and time: 46200 Sec to 84400 Sec) at 0.05 C.

DFT Studies: As per the references,[S1-S4] explicitly discuss representative DFT studies of Fe–N–C single-atom catalysts in Li–S chemistry. Song et al.[S1] Andritsos et al.[S2] works consistently show that Fe–Nx centers (including Fe–N_4 and coordinatively defective Fe–Nx and Fe–Ox sites) exhibit much stronger adsorption of Li_2S_n species and significantly reduced energy barriers for Li_2S nucleation and decomposition compared with non-metal or undoped carbon hosts. The calculated binding energies and transition-state barriers demonstrate that Fe–N–C sites can stabilize key polysulfide intermediates, promote reversible cleavage/formation of S–S and Li–S bonds, and thereby accelerate the Li_2S/LiPS conversion kinetics.[S3,S4] These reference DFT results are fully consistent with our experimental observations of reduced charge-transfer resistance, lower polarization, and enhanced rate performance in the S@Fe–MoS_2/SnS_2 cathode, supporting our conclusion that Fe–N–C sites act as highly active catalytic centers for Li–S redox.

The FFT was performed on selected high-resolution regions of the TEM image (not on the full image), using ImageJ's FFT plugin, and the corresponding d-spacings were extracted from the FFT patterns. Location of the FFT figure: The FFT analysis image with annotated d-spacing values has been included as a new figure in the Supporting Information (Fig. S18), alongside Table S1 which lists the measured d-spacing values for all identified phases (S_8, MoS_2, SnS_2, and graphitic C). Region of FFT analysis: The FFT was not performed on the full TEM image. Instead, we selected small, well-resolved crystalline regions (~5–10 nm^2) from the HRTEM image that showed clear lattice fringes. Each FFT was performed on an individual crystalline domain, allowing us to extract d-spacing values specific to that region. Local phase assignment in Figure 2d–e: The local assignment of S_8, MoS_2SnS_2, and Fe-N-C in the HRTEM images was performed as follows: For each region of interest in the HRTEM image, we performed localized FFT analysis on the lattice fringes visible in that specific area. The d-spacing values obtained from the FFT were then matched to the characteristic lattice planes of the constituent phases: MoS_2 (002) at 0.62 nm, MoS_2 (100) at 0.27 nm, SnS_2 (001) at 0.59 nm, SnS_2 (100) at 0.32 nm, graphitic C (002) at 0.34 nm, α-S_8 (040) at 0.34 nm, α-S_8 (222) at 0.37 nm, and α-S_8 (113) at 0.31 nm.

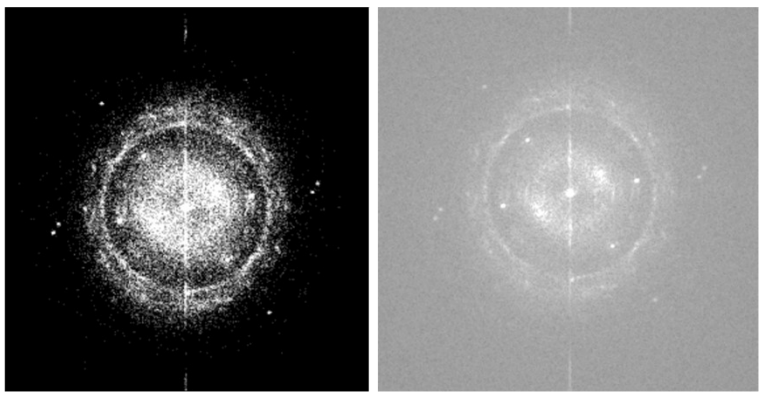

Fig. 18. Fast Fourier transform (FFT) analysis image of S@Fe-MoS_2/SnS_2.

The assignment of Fe-N-C (amorphous carbon domains with atomically dispersed Fe) was based on the absence of long-range lattice fringes in certain regions, combined with the presence of bright dots in HAADF-STEM images (Fig. 1d) corresponding to individual Fe atoms. Cross-validation: The phase assignments from localized FFT analysis are further corroborated by: (i) powder XRD, which confirms the presence of crystalline S_8, MoS_2, and SnS_2; (ii) Raman spectroscopy, which shows characteristic peaks for S_8, MoS_2, SnS_2, and the D/G bands of graphitic C; and (iii) HAADF-STEM-EDX elemental mapping (Fig. S5), which demonstrates the spatial distribution of S, Mo, Sn, Fe, N, and C across the composite.

Table S1. d-spacing values of S@Fe-MoS_2/SnS_2.

Sample	**Plane**	**d-spacing (nm)**
MoS_2	(002)	0.62
MoS_2	(100)	0.27
SnS_2	(001)	0.59
SnS_2	(100)	0.32
Graphitic C	(002)	0.34
α-S	(040)	0.34
α-S	(222)	0.37
α-S	(113)	0.31
Fe	(110)	0.20

Table S2. Performance comparison of representative Fe SAC-based cathodes for Li–S systems reported in previous studies.

S. No	Cathode	Initial Capacity	Number of Cycles	Capacity Retention	Rate Capability	References
1	FeSA-PCNF	1183 mA h g^{-1} at 0.2 C	500	76%	0.2–5C	S5
2	FeN_2–NC	900 mAh g^{-1} at 0.2 C	500	56%	0.1-5C	S6
3	FeTe/NC	1180 mAh g^{-1} at 0.2 C	1000	60%	0.1-5C	S7
4	Fe-N5/NC	1519 mAh g^{-1} at 0.1C	2000	36%	0.1-2C	S8
5	C_3N_4-Fe@rGO	1197.1 mAh g^{-1} at 0.2 C	900	37%	0.2-5C	S9
6	FeN_2C_2–SOx–NC	1297.1 mAh g^{-1} at 0.2 C	500	67%	0.1-4C	S10
7	Fe–Co DACs	1227 mAh g^{-1} at 0.2 C	1000	82%	0.1-5C	S11
8	MoS_2/SnS_2	1477 mA h g^{-1} at 0.05 C and	1000	40%	0.05-2C	Present work
9	Fe-MoS_2/SnS_2	1622 mA h g^{-1} at 0.05 C	1000	42%	0.05-2C	Present work

References

S1 Y. Song, L. Zou, C. Wei, Y. Zhou, Y. Hu, *Carbon Energy* 2023, **5**, e286.

S2 E. I. Andritsos, C. Lekakou and Q. Cai, *J. Phys. Chem. C* 2021, **125**, 18108-18118.

S3 W. Jing, Q. Tan, Y. Duan, K. Zou, X. Dai, Y. Song, M. Shi, J. Sun, Y. Chen, Y. Liu, *Small*, 2023, **19**, 2204880.

S4 J. Wang, W. Qiu, G. Li, J. Liu, D. Luo, Y. Zhang, Y. Zhao, G. Zhou, L. Shui, X. Wang, Z. Chen, *Energy Storage Mater.* 2022, **46**, 269-277.

S5 G. Zhao, Q. Chen, L. Wang, T. Yan, H. Li, C. Yuan, J. Mao, X. Feng, D. Sun, L. Zhang, *J. Mater. Chem. A.* 2022, **10**, 19893-19902.

S6 J. Wang, W. Qiu, G. Li, J. Liu, D. Luo, Y. Zhang, Y. Zhao, G. Zhou, L. Shui, X. Wang, Z. Chen, *Energy Storage Mater.* 2022, **46**, 269-277.

S7 J. Guo, L. Chen, L. Wang, K. Liu, T. He, J. Yu, H. Zhao, *Nano-Micro Lett.* 2025, **18**, 31.

S8 H. Xiao, K. Li, T. Zhang, X. Liang, F. Zhang, H. Zhuang, L. Zheng and Q. Gao, *Chem. Eng. J.* 2023, **471**, 144553.

S9 J. Wang, J. Wang, Y. Zhang, C. Ma, J. Wang, W. Qiao, L. Ling, *J. Mater. Sci. Techn.* 2025, **209**, 230-239.

S10 G. Cao, X. Li, L. Chen, R. Duan, J. Li, Q. Jiang, J. Wang, M. Li, M. Li, J. Wang, Y. Xi, W. Li, J. Peng, *Small*, 2024, **20**, 2311174.

S11 X. Sun, Y. Qiu, B. Jiang, Z. Chen, C. Zhao, H. Zhou, L. Yang, L. Fan, Y. Zhang, N. Zhang, *Nat. Comm.* 2023, **14**, 291.